INTERNATIONAL JOURNAL OF
Minerals, Metallurgy and Materials

Volume 31, Number 2, February 2024
Page 405

Research Article

https://doi.org/10.1007/s12613-023-2692-8

Lattice Boltzmann simulation study of anode degradation in solid oxide fuel cells during the initial aging process

Shixue Liu[1,2)✉], *Zhijing Liu*[1,2)], *Shuxing Zhang*[1,2)], *and Hao Wu*[1,2)]

1) Hydrogen Energy Industrial Technology Innovation Center, China Nuclear Power Technology Research Institute, Shenzhen 518031, China
2) Shenzhen Engineering Research Center for Hydrogen Safety, Shenzhen 518031, China

(Received: 25 May 2023; revised: 4 June 2023; accepted: 15 June 2023)

Abstract: For present solid oxide fuel cells (SOFCs), rapid performance degradation is observed in the initial aging process, and the discussion of the degradation mechanism necessitates quantitative analysis. Herein, focused ion beam-scanning electron microscopy was employed to characterize and reconstruct the ceramic microstructures of SOFC anodes. The lattice Boltzmann method (LBM) simulation of multiphysical and electrochemical processes in the reconstructed models was performed. Two samples collected from industrial-size cells were characterized, including a reduced reference cell and a cell with an initial aging process. Statistical parameters of the reconstructed microstructures revealed a significant decrease in the active triple-phase boundary and Ni connectivity in the aged cell compared with the reference cell. The LBM simulation revealed that activity degradation is dominant compared with microstructural degradation during the initial aging process, and the electrochemical reactions spread to the support layer in the aged cell. The microstructural and activity degradations are attributed to Ni migration and coarsening.

Keywords: solid oxide fuel cell; anode degradation; focused ion beam-scanning electron microscopy; lattice Boltzmann method

1. Introduction

Solid oxide fuel cell (SOFC) anodes are porous ceramic materials, mainly using Ni–yttria stabilized zirconia (Ni-YSZ) material. The porous anode provides a pathway for the transport of fuel from gas channels to the anodic functional layer as well as for electron and ion conduction [1]. Electrochemical reactions occur on the triple-phase boundary (TPB) region of the electrodes, mainly in the functional layer close to the electrolyte [2]. The degradation of SOFC anodes is related to the evolution of microstructural parameters, such as porosity, tortuosity, Ni and YSZ particle size, and TPB length [3–5].

Three-dimensional (3D) focused ion beam-scanning electron microscopy (FIB-SEM) has been used to analyze the microstructure of anodes with an accuracy of tens of nanometers. Sumi *et al*. [6] studied the effect of redox cycling on the electrolyte-supported Ni-YSZ button anode and found that anode degradation was primarily due to TPB length reduction. Vivet *et al*. [7], Iwai *et al*. [8], and Brus *et al*. [9] studied the method of estimating electronic and ionic conductivities and tortuosity based on reconstructed microstructures. Jiao *et al*. studied the anode degradation of electrolyte-supported button cells and found that polarization resistance increases due to Ni coarsening [10]. The authors also studied the effect of sintering temperature [11] and reduction temperature [12] on the anode performance degradation. Trini *et al*. studied the changes in the microstructural characterization of a cell extracted from a long-term-tested solid oxide electrolysis cell (SOEC) stack [13] and compared cells operating with SOFC and SOEC modes [14]. Most work has been conducted on easily-prepared electrolyte-supported button cells, except for those used in SOEC studies [13–14]. Yang *et al*. studied the degradation of an anode supported button cell, and found the Ni depletion decreased the average TPB density in anode active area [15]. Due to the difference in the sintering process between electrolyte-supported button cells and industrial-size anode-supported cells, the formation and evolution of microstructural patterns in anodes may also be different. Herein, we focus on industrial-size anode-supported cells.

In conventional computational fluid dynamic calculations of SOFC electrodes, porosity, tortuosity, and TPB length density are usually fixed as average values, and pore and particle size variations in the electrodes are not simulated. The pore and particle information can be obtained through FIB-SEM [2,16] and simulated by the lattice Boltzmann method (LBM). The LBM simulation can be employed for the multiphysical simulations of complex structures, particularly porous media [17]. In LBM iteration, variables on a lattice point depend only on its neighbors, and the linear scalability reduces computational complexity [18]. In addition, LBM is flexible for setting complex boundaries of a porous structure [17], such as SOFC electrodes [17–22]. Grew *et al*.

✉ Corresponding author: Shixue Liu E-mail: liushixue@cgnpc.com.cn

[18–19] performed LBM simulations using anode models from tomographic reconstruction; however, their two-dimensional models had less resolutions. Shikazono's group performed LBM simulations to predict polarization characteristics using 3D reconstructed microstructures obtained using FIB-SEM [20–22]. In their work, the simulations were performed to replicate physical and electrochemical processes in porous media and fit experimental curves under different operating conditions, and the degradation mechanism during redox cycles was discussed [22]. At present, LBM simulations have several open-source codes, such as OpenLB, MP_LABS, Palabos, and EI'Beem.

Rapid degradation due to the initial aging process was observed in the industrial-size cells [23]. The degradation mechanism has been qualitatively discussed through experimental microscopies; however, quantitative discussion is lacking. Generally, performance degradation is attributed to Ni coarsening and TPB length reduction; however, the extent of the effect of structural evolution on performance degradation remains unclear. Herein, LBM calculations were carried out based on a reconstructed 3D model of porous anodes. In addition, gas transportation through the pores and charge transfer through Ni or YSZ were simulated, and various physical field distributions were determined. Furthermore, the effects of structural evolution and activity degradation on the performance of anodes were quantitatively distinguished and discussed.

2. Method

2.1. Experimental

As shown in our previous work [23], an aged cell and a reference cell were tested and analyzed. The overall size of the cells is 12.4 cm × 12.4 cm, and the effective working area defined by the cathode area is 10 cm × 10 cm. The cells consist of Ni-YSZ, YSZ, gadolinium-doped ceria (GDC), and $La_{1-x}Sr_xCo_{1-y}Fe_yO_{3-\delta}$ (LSCF)-GDC layers as the anode, electrolyte, interlayer, and cathode, respectively. The reference cell was reduced for 5 h with humidified hydrogen (97mol% H_2 and 3mol% H_2O) at 720°C. The aged cell was operated for 40 h with 0.5 L/min humidified hydrogen and 1.5 L/min air at 740°C after 5-h reduction and 32-h activation. Electrochemical impedance spectra (EIS) were measured under different DC biases and analyzed on the basis of the distribution of relaxation times (DRT), and subsequent equivalent circuit model (ECM) fitting was employed to identify the contribution of individual processes. The detailed DRT calculation and ECM fitting results can be seen in our published paper [23].

The two observed samples were collected from two cells along the midline and approximately 2 cm from the left-side fuel inlet (Fig. 1). During pretreatment, the samples were infiltrated with epoxy resin under vacuum conditions, and most of the pores in the porous electrodes were filled with the epoxy resin. Then, the samples were observed through FIB-SEM (CB 540, manufactured by Carl Zeiss AG, Germany). The acceleration voltage of the FIB beam is 30 kV, and that of the in-lens secondary electron detector is 1.5 kV. Cross-sectional images with a resolution of 30 nm/pixel were obtained with an interval of 30 nm. Nearly 500 SEM images were scanned for each sample from the electrolyte–anode interface to the anode.

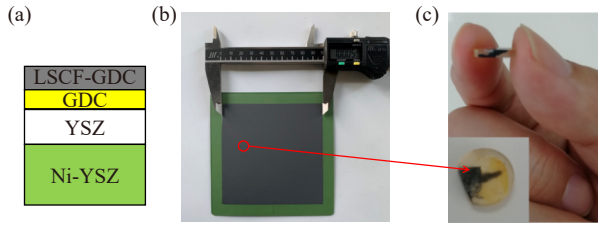

Fig. 1. (a) Schematic of four cell layers, (b) aged cell with the sampling point after the operation, and (c) a sample after pretreatment for focused ion beam-scanning electron microscopy.

The anode samples were virtually reconstructed by AVIZO software based on the SEM images. The three phases, namely Ni or NiO, YSZ, and pore, were distinguished with a threshold of image brightness. The phase volume fraction and TPB length in the reconstructed structures were obtained by using built-in formulas. The connected parts of Ni, YSZ, and pores were extracted after identifying the isolated phase.

2.2. Numerical method

2.2.1. Computational domain

Fig. 2 shows the schematic model used in the LBM simulation. A virtual electrolyte layer was set on the left surface of the reconstructed microstructure, where the actual anode–electrolyte interface is located. A virtual current collector was set on the right side to provide an electronic current flow boundary. Microstructure evolution during the initial aging process was simulated using the reference cell and the aged cell in this work. In constructing the contrasting phase interface, ball dilation with a size of 1 pixel was processed for the Ni phase. The reconstructed size for LBM simulation in the reference cell and aged cell is 24.0 μm × 14.04 μm × 11.04 μm and 24.6 μm × 13.08 μm × 11.04 μm, respectively. Limited by our computational resources, the simulated microstructures were rescaled from an initial voxel size of 30 to 120 nm during LBM simulations (Table 1).

2.2.2. Governing equations

Hydrogen and water steam gas diffusion, as well as electron and oxygen ion conduction, were simulated in the porous microstructure.

The dusty gas model was used to describe gas diffusion [20]:

$$\frac{N_i}{D_{i,\mathrm{k}}}+\sum_{j\neq i}\frac{y_jN_i-y_iN_j}{D_{i,j}}=-\frac{\nabla p_i}{RT} \tag{1}$$

where N_i, y_i, and p_i are the molar flux, molar fraction, and partial pressure of gas species i. $D_{i,\mathrm{k}}$ and $D_{i,j}$ are the Knudsen and binary diffusion coefficients, respectively. Subscripts i and j represent gas species i and j, and subscript k represents Knudsen diffusion. R and T are gas constant and gas temperature. Only H_2 and H_2O were considered herein in accordance with the experimental condition.

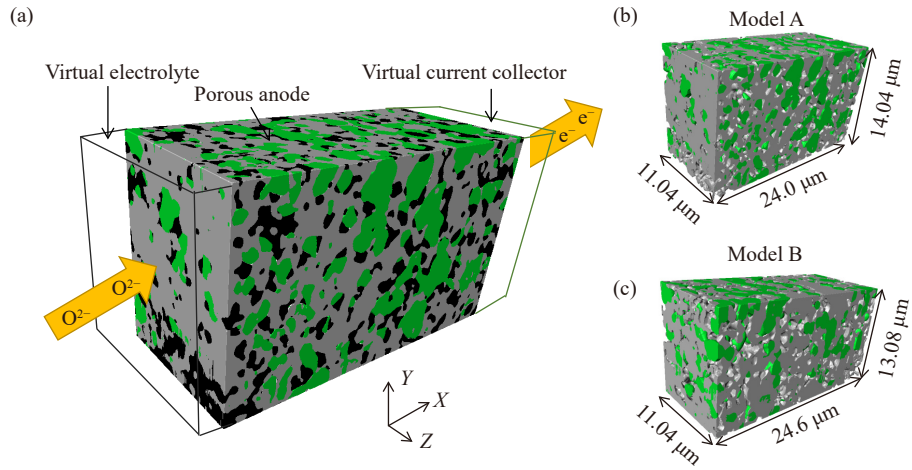

Fig. 2. (a) Schematic of the computational model; simulated porous region of (b) model A reconstructed from the reference cell, and (c) model B reconstructed from the aged cell. Green: Ni; Gray: YSZ; Black: pore.

Table 1. Number of voxels for the reconstructed region and in LBM calculations

Before and after rescale	Model A	Model B
Reconstructed region (Voxel size = 30 nm)	800 × 468 × 368	820 × 436 × 368
Rescaled in LBM (Voxel size = 120 nm)	200 × 117 × 92	205 × 109 × 92

The electron and oxygen ion conduction equations can be expressed as follows:

$$\nabla\cdot(\sigma_{el}\nabla\tilde{\mu}_{e^-}) = -i_{TPB} \tag{2}$$

$$\nabla\cdot(\sigma_{ion}\nabla\tilde{\mu}_{O^{2-}}) = i_{TPB} \tag{3}$$

where σ_{el}, σ_{ion}, $\tilde{\mu}_{e^-}$, $\tilde{\mu}_{O^{2-}}$, and i_{TPB} indicate the electronic conductivity, ionic conductivity, electrochemical potential of electron, electrochemical potential of oxygen ion, and current density on the triple-phase boundary, respectively.

The linear current density on local TPB is expressed by using the Butler–Volmer equation [20],

$$i_{TPB} = i_{0,TPB}L_{TPB}\left[\exp\left(-\frac{2F\eta_{act}}{RT}\right) - \exp\left(-\frac{F\eta_{act}}{RT}\right)\right] \tag{4}$$

where $i_{0,TPB}$, L_{TPB}, F, and η_{act} are the local exchange current density, local active TPB density, Faraday's constant, and local activation polarization, respectively.

The exchange current density is calculated using the following equation:

$$i_{0,TPB} = i^*_{0,TPB}\left(\frac{p_{H_2}}{p_0}\right)^{\alpha}\left(\frac{p_{H_2O}}{p_0}\right)^{\beta}\exp\left(-\frac{E_a}{RT}\right) \tag{5}$$

where p_{H_2}, p_{H_2O}, and p_0 indicate the partial pressure of H_2, H_2O and the reference pressure, respectively. $i^*_{0,TPB}$ is the fitting parameter in LBM calculation. The exponential factors α and β are set as −0.03 and 0.4, respectively, and the anodic reaction activation energy, E_a, is set as 152 kJ [20].

The local activation polarization, η_{act}, can be defined as follows [21]:

$$\eta_{act} = -\frac{1}{2F}\left\{2\tilde{\mu}_{e^-,Ni-YSZ} - \tilde{\mu}_{O^{2-},Ni-YSZ} + \left[\Delta G^{\ominus} + RT\ln\frac{p_{H_2O}}{p_{H_2}}\right]_{local}\right\} \tag{6}$$

where $\tilde{\mu}_{e^-,Ni-YSZ}$, $\tilde{\mu}_{O^{2-},Ni-YSZ}$, and $\Delta G^{\ominus}$ indicate the electron and oxygen ion electrochemical potential on the interface of Ni and YSZ particles, and standard Gibbs free energy, respectively. The subscript local indicates the local gas composition at the vicinity of TPB.

In fitting the current density dependence on the anode overpotential, the anode overpotential can be calculated as follows [21]:

$$\eta_{anode} = -\frac{1}{2F}\left\{2\tilde{\mu}_{e^-,anode-CC} - \tilde{\mu}_{O^{2-},anode-CC} + \left[\Delta G^{\ominus} + RT\ln\frac{p_{H_2O}}{p_{H_2}}\right]_{CC}\right\} \tag{7}$$

where $\tilde{\mu}_{e^-,anode-cc}$ and $\tilde{\mu}_{O^{2-},anode-cc}$ indicate the electron and oxygen ion electrochemical potential on the interface of the porous anode and the virtual current collector. The subscript CC indicates the position at the virtual current collector. The average hydrogen and steam pressures at the virtual current collector are used in this equation.

The parameters used in the equations are summarized in Table 2. The temperature and pressure are the same as the experimental conditions in Ref. [23]. In addition, the fuel composition setting is the same as the inlet gas because the sampling point is near the fuel inlet. For the boundary conditions, a constant-gas composition boundary is applied on the virtual current collector surface, and constant electronic and ionic current fluxes are imposed on the virtual current collector and virtual electrolyte, respectively.

2.2.3. LBM solver

The LBM was used to solve the governing equations of gas diffusion and charge conduction. The simplest lattice Bhatnagar–Gross–Krook D3Q6 model was adopted as the discrete model of the LBM in this study [21].

$$f_m(x + c_m\Delta t, t + \Delta t) = f_m(x,t) - \frac{1}{t^*}[f_m(x,t) - f_m^{eq}(x,t)] + w_m\Delta t \tag{8}$$

Table 2. Parameter values in the simulation model

Parameter	Value
Temperature, T / K	1013
Total pressure, p / Pa	101325
Fuel composition	97mol% H_2 and 3mol% H_2O
YSZ ionic conductivity [20], σ_{ion} / (S·m^{-1})	$3.34 \times 10^4 \exp(-10300/T)$
Ni electronic conductivity [20], σ_{el} / (S·m^{-1})	$3.27 \times 10^6 - 1065.3T$

where f_m, c_m, w_m, f_m^{eq} indicate the density distribution function, velocity, reaction production and the Maxwellian local equilibrium distribution in the mth direction; x, t, t^*, and Δt indicate position, time, relaxation time, and time step, respectively. The outside boundary surfaces, except for the electrolyte–anode interface and anode–current collector interface, were set as the zero-gradient boundary condition. At the phase interface inside the simulation model, a no-flux boundary condition was imposed for the governing equations.

3. Results and discussion

3.1. Reconstructed microstructure

Following 3D reconstruction, the quantified parameters were calculated, as summarized in Table 3. Total volume fractions of the pore, YSZ, and Ni slightly vary before and after the short-term aging. This indicates that the material compositions of different cells from the same production batch are uniform, and the reconstructed cells are large enough that the effects of local large particles can be neglected. However, the volume fractions in the functional layers differ from the total values. The Ni volume fraction decreased in the functional layers, and the pore volume fraction increased. This phenomenon results in a large total TPB length density in the functional layer, which indicates good output performance.

Table 3. Volume fraction, connectivity, and triple-phase boundary length density of the reference cell and aged cell after three-dimensional reconstruction

Cell	Region	Volume fraction / vol%			Connectivity / vol%			TPB length density / (μm·μm^{-3})	
		Pore	YSZ	Ni	Pore	YSZ	Ni	Total	Active
Reference cell	Reconstructed[a]	21.6	47.9	30.5	91.6	99.7	97.6	2.14	1.66
	FL[b]	26.8	50.6	22.6	98.5	99.9	90.5	2.48	1.93
Aged cell	Reconstructed[a]	22.8	50.5	26.9	98.4	99.8	82.2	1.42	1.09
	FL[b]	25.6	51.9	22.7	98.1	99.9	62.8	1.81	1.01

Note: [a] The total reconstructed region. [b] The function layer, ~4 μm from the anode–electrolyte interface.

In the reconstructed microstructures, isolated Ni particles were observed, which do not allow the electrons from the external circuit to be transferred; therefore, the isolated Ni particles were considered inactive for electrochemical reactions. The YSZ and pore phases exhibited similar behaviors. The isolated phases were observed in the reference and aged cells (Figs. 3 and 4). The connected phase fraction was used to characterize the connectivity of each phase of the reconstructed structures, and the results are summarized in Table 3. The electrochemical testing results of the two cells can be found in our previously published paper [23]. Further, the rapid degradation during the initial aging process was attributed to Ni migration in the functional layer. The connectivity of the pore and the YSZ phase in the functional layers is >98vol% for both samples, while that of the Ni phase in the functional layers is 90.5vol% and 62.8vol% in the reference and aged cells, respectively. This indicates that a large number of Ni particles in the functional layer of the aged cell were isolated, and the active TPB length density in functional layers was reduced more than that in the total reconstructed region. The Ni volume fraction in the functional layers is almost the same in both cells; thus, the significant drop in TPB length density in the aged cell is due to decreased Ni connectivity. A comparison of the Ni morphology shown in Figs. 3 and 4 reveals that the Ni particle sizes increased in connected and isolated phases in the aged cell, indicating that Ni coarsening existed and led to the morphological changes in formation of the isolated phase.

3.2. LBM fitting

Table 4 summarizes the microstructural parameters that were identified in the LBM code. Considering that the Ni phase has been processed with a ball dilation of 1 pixel from the initially reconstructed structures, the Ni volume fraction increased as compared with that presented in Table 3. The TPB length density is consistent with that obtained by AVIZO.

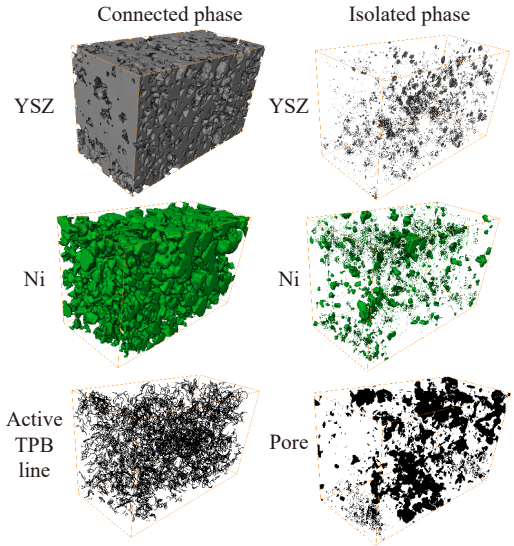

Fig. 3. Connected phase, isolated phase, and the active triple-phase boundary lines in the reference cell.

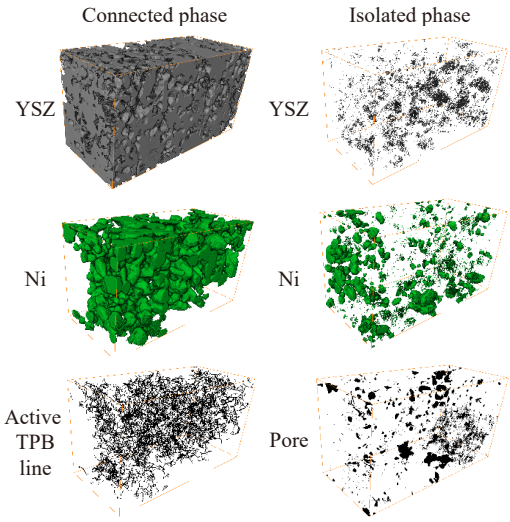

Fig. 4. Connected phase, isolated phase, and the active triple-phase boundary lines in the aged cell.

As analyzed in Ref. [23], the EIS was separated into individual polarization resistance by ECM, and the anodic overpotential included voltage loss from R_1–R_5 and R_S. Here R_1 and R_2 correspond to anode charge transfer reactions and ionic transport processes near TPB, R_3 corresponds to the voltage loss at the cathode, R_4 and R_5 correspond to gas diffusion through a 550-μm anode, and R_S corresponds to Ohmic resistance, resulting primarily from the electrolyte. The current LBM model only includes an anode thickness <30 μm, and the anode overpotential includes only the voltage loss from R_1 and R_2.

The fitting parameter in the exchange current density of Eq. (5) was adjusted to comply with the experimental data (Fig. 5). The fitted exchange current density was 1.75×10^{-4} A/m for the aged cell data, and the root mean square error was 4.9%. The experimental data before the initial aging process was simulated with model A from the reference cell, and the fitted exchange current density was 7.63×10^{-4} A/cm.

Table 4. Volume fraction, connectivity, and triple-phase boundary length density identified in lattice Boltzmann method code for model A and model B

Model	Volume fraction / vol%			Connected phase fraction / vol%			TPB length density / (μm·μm^{-3})
	Pore	YSZ	Ni	Pore	YSZ	Ni	Active
Model A	21.3	42.9	35.8	89.3	99.7	97.6	1.48
Model B	22.4	46.5	31.2	97.2	99.8	89	0.97

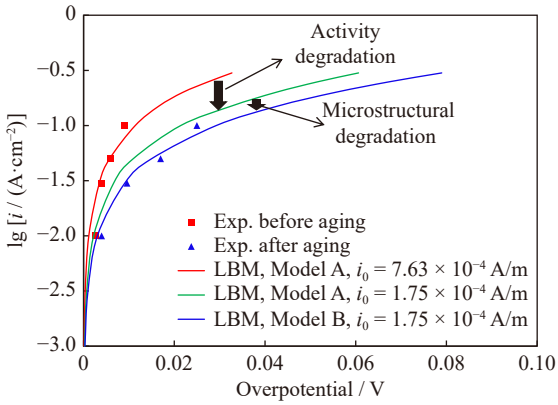

Fig. 5. Comparison of the lattice Boltzmann method results with the experimental data.

3.3. Degradation during the initial aging process

While quantitatively evaluating the effect of the exchange current density and microstructure, an exchange current density (i_0) of 1.75×10^{-4} A/m was used for model A, and the simulated green curve was between the two fitting curves, as shown in Fig. 5. The gap between the red and green lines is defined as the activity degradation because the geometric models are the same, and the fitting exchange current density is different for the two curves. Similarly, the gap between the green and blue lines is defined as microstructural degradation, which is due to the geometric model change. It is observed that the gap corresponding to activity degradation is wider than that corresponding to microstructural degradation. The result shows that performance degradation can be classified into activity and microstructural degradations, and the activity degradation of the local TPB is dominant.

The microstructural degradation can be attributed to decreased TPB length and Ni connectivity. During the aging process, Ni migration from the functional layer to the support layer and Ni coarsening lead to a decreased TPB length and Ni connectivity in the functional layer [23–24]. The activity of the local TPB is related to the activity of a series of elementary reactions on the Ni-YSZ surface. The reaction barriers of elementary reactions can be affected by Ni particle sizes and the surface orientation of Ni and YSZ surfaces near TPB, which has been confirmed through DFT calculations [25–29]. Therefore, Ni migration and coarsening can reduce not only the TPB length and Ni connectivity but also the local activity.

3.4. Ionic electrochemical potential and current density distribution

The ionic electrochemical potential distribution in YSZ materials of models A and B at a current density of 0.1 A/cm^2 is shown in Fig. 6. The distribution is inhomogeneous in the *Y*–*Z* cross-section because of the porous structures. The electrochemical potential decreases along the *X* direction, and the reduced range in the aged cell is larger, resulting in a larger Ohmic polarization.

The distribution of the ionic current density (i_{ionic}) over the *Y*–*Z* cross-section is heterogeneous, and the average value is calculated as shown in Fig. 7. In model A, more than 90% of the ionic current is transferred to the electronic current in the functional layer. In contrast, the ionic current density varies

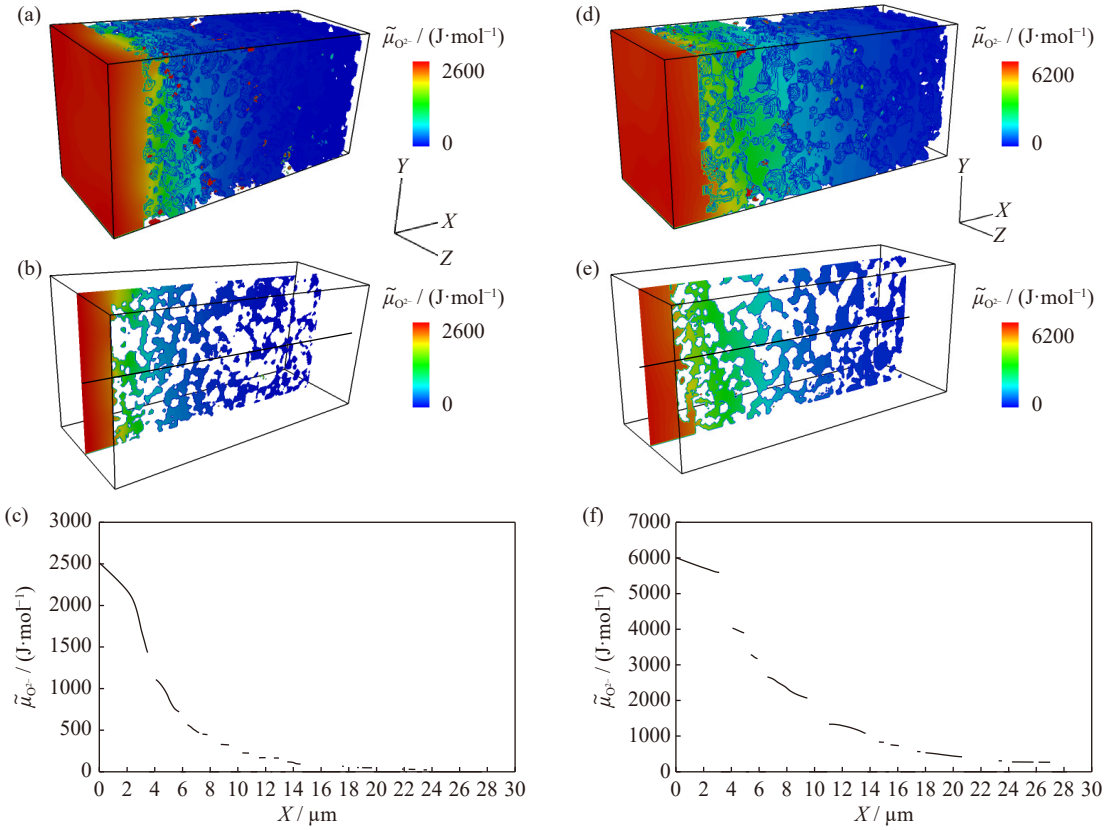

Fig. 6. Ionic electrochemical potential three-dimensional distribution, surface distribution, and line distribution in the middle line along the X direction in YSZ of (a–c) model A and (d–f) model B at a current density of 0.1 A/cm^2.

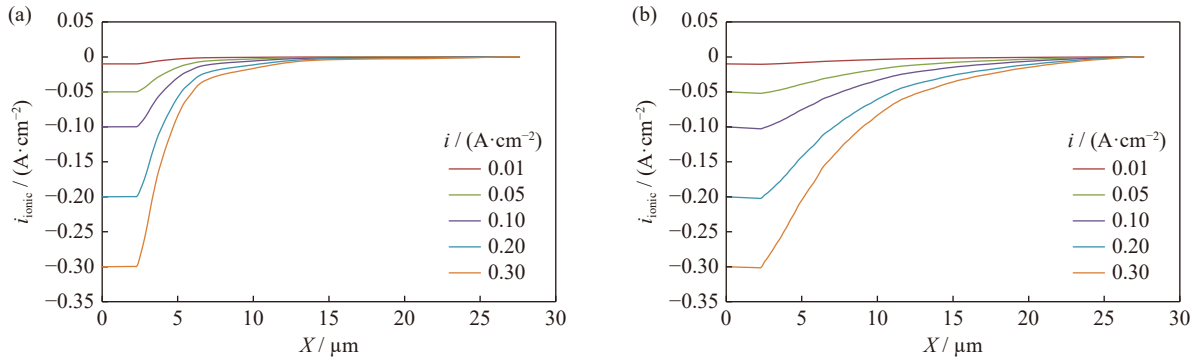

Fig. 7. Ionic current density along the *X* direction for different performance outputs in (a) model A and (b) model B.

slowly along the *X* direction in the aged cell. This indicates that the functional layer of the aged cell cannot provide enough active TPB, and more ionic current is transferred to the anode support layer, leading to higher Ohmic losses.

4. Conclusion

FIB-SEM was employed to reconstruct the microstructures of samples obtained from industrial-size SOFC single cells. The quantitative results of volume fraction and TPB length distribution were recorded for the reduced cell and the initially aged cell. The TPB length and Ni connectivity decreased during the short-term aging. LBM simulations revealed that performance degradation comprises microstructural and TPB activity degradations, and the latter dominates in the initial aging process. Ni migration and coarsening can not only decrease the TPB length and Ni connectivity but also decrease the local activity. The functional layer of the aged cell cannot provide enough active TPB, and the charge transfer reactions spread to the anode support layer.

Acknowledgements

This work was financially supported by the National Key R&D Program of China (No. 2018YFB1502201) and the Guangdong Basic and Applied Basic Research Foundation, China (No. 2020A1515010551). The authors acknowledge Dr. Yu Wang from the Shanghai Institute of Applied Physics for the FIB-SEM test. The numerical calculations in this paper have been done on the supercomputing system in the Supercomputing Center of University of Science and Technology of China.

Conflict of Interest

All the authors declare that there is no conflict of interest regarding the publication of this paper.

References

[1] S.C. Singhal, and K. Kendall, *High-temperature Solid Oxide Fuel Cells*: *Fundamentals*, *Design and Applications*, Elsevier, New York, 2003.

[2] S.X. Liu, C. Song, and Z.J. Lin, The effects of the interconnect rib contact resistance on the performance of planar solid oxide fuel cell stack and the rib design optimization, *J. Power Sources*, 183(2008), No. 1, p. 214.

[3] Q.P. Fang, L. Blum, and D. Stolten, Electrochemical performance and degradation analysis of an SOFC short stack following operation of more than 100, 000 hours, *J. Electrochem. Soc.*, 166(2019), No. 16, p. F1320.

[4] A. Hauch and M. Mogensen, Ni/YSZ electrode degradation studied by impedance spectroscopy: Effects of gas cleaning and current density, *Solid State Ionics*, 181(2010), No. 15-16, p. 745.

[5] S. Koch, P.V. Hendriksen, M. Mogensen, *et al*., Solid oxide fuel cell performance under severe operating conditions, *Fuel Cells*, 6(2006), No. 2, p. 130.

[6] H. Sumi, R. Kishida, J.Y. Kim, H. Muroyama, T. Matsui, and K. Eguchi, Correlation between microstructural and electrochemical characteristics during redox cycles for Ni–YSZ anode of SOFCs, *J. Electrochem. Soc.*, 157(2010), No. 12, art. No. B1747.

[7] N. Vivet, S. Chupin, E. Estrade, *et al*., 3D Microstructural characterization of a solid oxide fuel cell anode reconstructed by focused ion beam tomography, *J. Power Sources*, 196(2011), No. 18, p. 7541.

[8] H. Iwai, N. Shikazono, T. Matsui, *et al*., Quantification of SOFC anode microstructure based on dual beam FIB-SEM technique, *J. Power Sources*, 195(2010), No. 4, p. 955.

[9] G. Brus, K. Miyawaki, H. Iwai, M. Saito, and H. Yoshida, Tortuosity of an SOFC anode estimated from saturation currents and a mass transport model in comparison with a real microstructure, *Solid State Ionics*, 265(2014), p. 13.

[10] Z.J. Jiao, N. Shikazono, and N. Kasagi, Quantitative characterization of SOFC nickel–YSZ anode microstructure degradation based on focused-ion-beam 3D-reconstruction technique, *J. Electrochem. Soc.*, 159(2012), No. 3, p. B285.

[11] Z.J. Jiao, G. Lee, N. Shikazono, and N. Kasagi, Quantitative study on the correlation between solid oxide fuel cell Ni–YSZ composite anode performance and sintering temperature based on three-dimensional reconstruction, *J. Electrochem. Soc.*, 159(2012), No. 7, p. F278.

[12] Z.J. Jiao and N. Shikazono, Quantitative study on the correlation between solid oxide fuel cell Ni–YSZ composite anode performance and reduction temperature based on three-dimensional reconstruction, *J. Electrochem. Soc.*, 162(2015), No. 6, p. F571.

[13] M. Trini, P.S. Jørgensen, A. Hauch, J.J. Bentzen, P.V. Hendriksen, and M. Chen, 3D microstructural characterization of Ni/YSZ electrodes exposed to 1 year of electrolysis testing, *J. Electrochem. Soc.*, 166(2019), No. 2, p. F158.

[14] M. Trini, A. Hauch, S. De Angelis, X. Tong, P.V. Hendriksen, and M. Chen, Comparison of microstructural evolution of fuel electrodes in solid oxide fuel cells and electrolysis cells, *J. Power Sources*, 450(2020), art. No. 227599.

[15] X. Yang, Z.H. Du, Q. Zhang, *et al*., Effects of operating conditions on the performance degradation and anode microstructure evolution of anode-supported solid oxide fuel cells, *Int. J. Miner. Metall. Mater.*, 30(2023), No. 6, pp. 1181-1189.

[16] H. Yakabe, M. Hishinuma, M. Uratani, Y. Matsuzaki, and I. Yasuda, Evaluation and modeling of performance of anode-supported solid oxide fuel cell, *J. Power Sources*, 86(2000), No. 1-2, p. 423.

[17] L. Chen, A. He, J.L. Zhao, *et al*., Pore-scale modeling of complex transport phenomena in porous media, *Prog. Energy Combust. Sci.*, 88(2022), art. No. 100968.

[18] K.N. Grew, A.S. Joshi, and W.K.S. Chiu, Direct internal reformation and mass transport in the solid oxide fuel cell anode: A pore-scale lattice boltzmann study with detailed reaction kinetics, *Fuel Cells*, 10(2010), No. 6, p. 1143.

[19] K.N. Grew, A.S. Joshi, A.A. Peracchio, and W.K.S. Chiu, Pore-scale investigation of mass transport and electrochemistry in a solid oxide fuel cell anode, *J. Power Sources*, 195(2010), No. 8, p. 2331.

[20] N. Shikazono, D. Kanno, K. Matsuzaki, H. Teshima, S. Sumino, and N. Kasagi, Numerical assessment of SOFC anode polarization based on three-dimensional model microstructure reconstructed from FIB-SEM images, *J. Electrochem. Soc.*, 157(2010), No. 5, art. No. B665.

[21] D. Kanno, N. Shikazono, N. Takagi, K. Matsuzaki, and N. Kasagi, Evaluation of SOFC anode polarization simulation using three-dimensional microstructures reconstructed by FIB tomography, *Electrochim. Acta*, 56(2011), No. 11, p. 4015.

[22] T. Shimura, Z.J. Jiao, and N. Shikazono, Evaluation of nickel-yttria stabilized zirconia anode degradation during discharge operation and redox cycles operation by electrochemical calculation, *J. Power Sources*, 330(2016), p. 149.

[23] Z.W. Lyu, S.X. Liu, Y.G. Wang, *et al*., Quantifying the performance evolution of solid oxide fuel cells during initial aging process, *J. Power Sources*, 510(2021), art. No. 230432.

[24] G.J. Nelson, K.N. Grew, J.R. Izzo Jr, *et al*., Three-dimensional microstructural changes in the Ni–YSZ solid oxide fuel cell anode during operation, *Acta Mater.*, 60(2012), No. 8, p. 3491.

[25] M. Shishkin and T. Ziegler, Oxidation of H_2, CH_4, and CO molecules at the interface between nickel and yttria-stabilized zirconia: A theoretical study based on DFT, *J. Phys. Chem. C*, 113(2009), No. 52, p. 21667.

[26] M. Shishkin and T. Ziegler, Hydrogen oxidation at the Ni/yttria-stabilized zirconia interface: A study based on density functional theory, *J. Phys. Chem. C*, 114(2010), No. 25, p. 11209.

[27] C.S. Cucinotta, M. Bernasconi, and M. Parrinello, Hydrogen oxidation reaction at the Ni/YSZ anode of solid oxide fuel cells from first principles, *Phys. Rev. Lett.*, 107(2011), No. 20, art. No. 206103.

[28] S.C. Ammal and A. Heyden, Combined DFT and microkinetic modeling study of hydrogen oxidation at the Ni/YSZ anode of solid oxide fuel cells, *J. Phys. Chem. Lett.*, 3(2012), No. 19, p. 2767.

[29] S. Liu, T. Ishimoto, D.S. Monder, and M. Koyama, First-principles study of oxygen transfer and hydrogen oxidation processes at the Ni–YSZ–gas triple phase boundaries in a solid oxide fuel cell anode, *J. Phys. Chem. C*, 119 (2015), p. 27603.